Dynamic fracture parameters and constraint effects in functionally graded syntactic epoxy foams

Medhat A. El-Hadek, Hareesh V. Tippur *

Department of Mechanical Engineering, 202 Ross Hall, Auburn University, Auburn, AL 36849-5341, USA

Received 18 May 2002; received in revised form 5 December 2002

Abstract

Functionally graded syntactic foam sheets are developed by dispersing microballoons in epoxy for studying dynamic fracture behavior under low velocity impact loading. The volume fraction of microballoons is graded linearly over the width of the sheets. The mode-I crack initiation and growth behaviors are studied using reflection coherent gradient sensing technique and high-speed photography in samples with crack on the compliant and stiff sides and oriented along the compositional gradient. Crack growth along the gradient in each case shows sudden acceleration followed by steady state growth and deceleration during the window of observation. In both cases, the crack accelerations are similar while crack decelerations show differences. The dynamic stress intensity factor history prior to crack initiation in each case shows a rapid increase at different rates with the crack on the compliant side of the graded sheet experiencing higher rate of loading relative to the one with the crack on the stiffer side. Post-crack initiation stress intensity factor histories suggest increasing fracture toughness with crack growth in the graded sample with the crack on the compliant side while a decreasing trend is seen when the crack is on the stiffer side.

Optical measurements are supplemented by finite element simulations for studying crack tip constraint effects on fracture behavior of graded foam sheets. Computed plane strain constraints in graded configurations are essentially identical to the homogeneous counterpart and the computed stress intensity factors obtained from plane stress elasto-dynamic analyses of the graded foams correlate well with the experimental measurements prior to crack initiation. The computed T-stress histories however, show an earlier loss of negative crack tip constraint in case of the graded foam sample with a crack on the compliant side. This correlates well with the higher crack tip loading rate and earlier crack initiation suggesting a possible role of in-plane constraint on fracture of graded foam. The coincidence of the time rate of change of in-plane constraint parameter becoming stationary close to experimentally observed crack initiation times are noted.

© 2002 Elsevier Science Ltd. All rights reserved.

Keywords: Syntactic foams; Functionally graded materials (FGM); Dynamic fracture; Optical measurements; CGS; T-stress; Constraint

---

* Corresponding author. Tel.: +1-334-844-3327.
  E-mail address: htippur@eng.auburn.edu (H.V. Tippur).

1. Introduction

Mechanical blending of microballoons with polymeric or metallic matrix materials result in a class of structural foams commonly referred to as syntactic foams. The porosity in these foams is typically at the microscopic level and can be relatively easily controlled. Additionally, unlike conventional foams, these do not exhibit macroscale material anisotropy. The microscopic porosity in these result in several mechanical property enhancements including specific strength, shear stiffness, impact resistance, and energy absorption (Shutov, 1986). Further, favorable thermal, dielectric and damping characteristics make these foams multifunctional as well. Hence, they have been considered for a variety of applications such as bulkheads of ships and submarines (Burcher, 1994), automotive and personnel protection (Koizumi, 1997), heat shielding of missile heads and aerospace structures.

At the moment relatively few studies on mechanical characterization of syntactic foams are available in the literature. Among the quasi-static studies, Huang and Gibson (1993) have reported measurement and modeling of elastic modulus of polyester syntactic foams. They have successfully compared their data with calculations based on dilute suspension of microballoons at low volume fractions. The elastic behavior of syntactic foams has been studied by Bardella and Genna (2001). For the specific type foam they have examined, it is concluded that the wall thickness of the microballoons have little influence on the overall elastic modulus and, estimation of elastic modulus using three-phase self-consistent model is shown to provide good agreement. An experimental–numerical investigation into the tensile, compressive and fracture behavior of pre-fabricated syntactic foams have been recently reported by Rizzi et al. (2000). They have presented several interesting results for this material based on homogenized properties at the macroscale and show good agreement between crack growth simulations based on Dugdale-type cohesive law and experiments. El-Hadek and Tippur (2002) have undertaken a detailed study of the elastic and fracture properties under quasi-static loading conditions for epoxy and urethane syntactic foams. For a specific type of syntactic foam, with microballoon wall thickness of $\approx$400 nm, they conclude that the microballoon wall has little to contribute towards tensile modulus since Hashin-Shtrikman lower-bound predictions for porous materials agree well with the measurements. They have also proposed and validated simple strain energy based models for predicting mode-I crack initiation toughness by treating syntactic foams as porous materials.

Among the dynamic studies, Scarponi et al. (1996) have undertaken impact testing of sandwich composite panels involving syntactic foam as the core and point out advantages of such constructions using post-impact compression tests of indented panels. Fabrication and impact behaviors of syntactic foams have been studied by Kim and Oh (2000), while compression failure has been examined by Gupta et al. (1999). Recently, El-Hadek and Tippur (2001) have demonstrated the feasibility of using optical intereferometry and high-speed photography to perform real-time deformation measurements in syntactic foam sheets subjected to impact loading.

In this paper, an experimental and numerical study on dynamic fracture of functionally or compositionally graded epoxy syntactic foams is presented. The primary focus of this research is on mode-I crack initiation and growth in pre-cracked foam sheets subjected to dynamic loading by one-point impact. Examination of the fracture behavior of compositionally or functionally graded syntactic foams, is aimed towards aiding in an eventual development of new concepts in energy barriers, sandwich constructions, and in understanding the benefits of graded porosity often found in biological systems. First, material preparation and elastic property characterization of epoxy syntactic foam sheets having spatially varying volume fraction of microballoons in the matrix is presented. This is followed by a brief description of the optical method used for studying dynamic crack initiation and growth. Subsequently, extraction of dynamic stress intensity factors is described and stress intensity factors and crack growth histories in different graded foams are compared. The finite element models are developed to supplement the experimental measurements and provide macro-mechanical explanations based on crack tip constraint or the so-called T-stress

(the second term or the coefficient of the r^0 term in the asymptotic expansion) on fracture behaviors in graded foam sheets. Potential role of T-stress and hence crack tip biaxiality on crack tip loading rate, crack initiation and growth behaviors in functionally graded foam sheets are deduced.

2. Experiments

2.1. Material preparation and characterization

Syntactic foams were prepared using microballoons and low viscosity amine cured epoxy resin. The microballoons used in this investigation were commercially available hollow soda-lime glass spheres of mean diameter 60 μm and wall thickness ≈400 nm. The extremely small wall thickness relative to the diameter of these fillers makes the cured mixture behave as a porous material (El-Hadek and Tippur, 2002). Low shrinkage and long duration room temperature curing profile of the chosen epoxy minimizes the residual stresses in the foam. Some relevant material properties of the constituents are listed in Table 1. The microballoons were suitably distributed in two-part epoxy system and were cast in PMMA molds. Room temperature curing of the mixture for 72 h yielded 8.8 mm thick foam sheets. Two different sets of foams were prepared—(a) homogeneous foam sheets of volume fraction $V_f = 0.25$, (b) compositionally graded foam sheets with microballoon volume fraction varying continuously between 0 and 0.45 along the width of the sheet.

The methodology followed in making graded foams consisted of preparing several different homogeneous epoxy–microballoon mixtures. The lowest volume fraction mixture was poured first into the bottom of the mold followed by the next higher volume fraction, and so on. A complex interplay of buoyancy and viscous forces on the microballoons along with thermal convection during polymerization results in a nearly linear and macroscopically continuous volume fraction gradient. The gradient extends over ≈42 mm, between a region of nearly pure epoxy at one end and microballoon-rich (pore-rich) epoxy (45% volume fraction of microballoons) at the other. Fig. 1(a) shows the linear gradient of the volume fraction of microballoons dispersion over the graded sheet. Accordingly, mechanical properties also vary in these specimens over the sample width. Previously, El-Hadek and Tippur (2002) have established look-up charts (see, Appendix A) for wave speeds and density for syntactic foams having homogeneous dispersion of microballoons at various different volume fraction levels. Using these charts in conjunction with local ultrasonic pulse-echo measurement of longitudinal and shear wave speeds at various locations along the width of the graded foam sheets, density and dynamic Young's modulus variations were determined. These are shown in Fig. 1(b) and (c), respectively. It should be noted that Poisson's ratio in these compositions were found to be nearly constant at 0.35 ± 0.01. Additionally, the ultrasonic transducer used had a radius of ≈2 mm, and hence the measurements represent averages values over the transducer size.

Table 1
Material properties

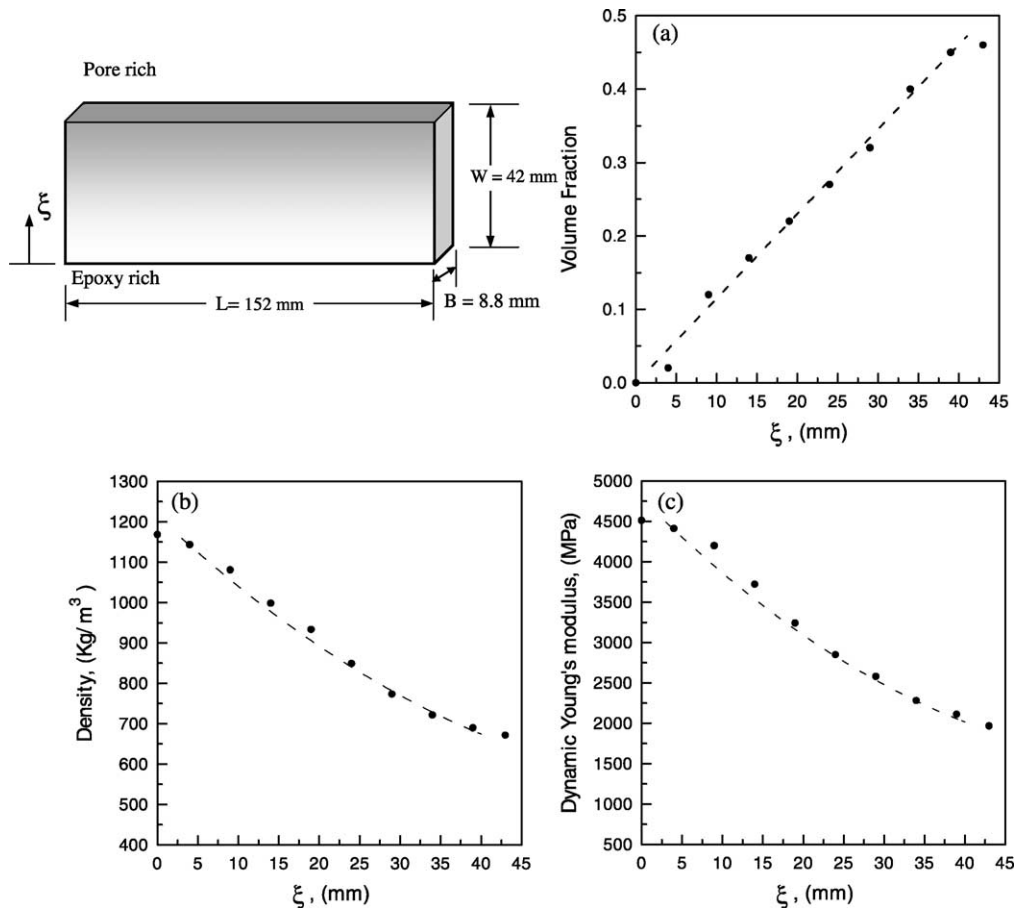| Properties	Microballoons	Epoxy
Mean size	∼60 μm	–
Wall thickness	∼400 nm	–
K_{Ic} (MPa $\sqrt{m}$) (static)	∼0.7	1.1 ± 0.1
Tensile modulus (MPa) (static)	–	3016
Tensile strength (MPa) (static)	–	58
Density (g/cc)	0.13	1.18
Viscosity (centipoises)	–	213

Fig. 1. Variation of (a) volume fraction, (b) density and (c) dynamic Young's modulus, in compositionally graded syntactic foam sheet castings.

The specimens for optical tests were machined from cast sheets to dimensions 152 mm × 42 mm × 8.8 mm. An 8 mm long edge notch (root radius ∼150 μm) was introduced in each specimen using high-speed diamond impregnated circular saw in the direction parallel to the compositional gradient in each specimen. A schematic of the cracked specimen geometry and the loading configuration is shown in Fig. 2(a). Among the graded specimens, two sets, one with crack on the compliant side ($E_2/E_1 > 1$) (subscripts 1 and 2 denote the values at the cracked edge and the impact edge of the sample, respectively as shown) of the sheet and the other with crack on the stiffer side ($E_2/E_1 < 1$) was prepared. The homogeneous counterparts ($E_2/E_1 = 1$) of the graded specimens with identical crack geometry were prepared for comparative study. These include foam samples having microballoon volume fraction of 0.25 as described earlier. It should be noted that the values of the longitudinal wave speed and the density of the 0.25 volume fraction homogeneous foam were approximately same as the corresponding *average* values over the width of the graded foam samples. The average wave speed values were determined over the width (W) of the sample as $C_{\mathrm{avg}} = \frac{1}{W} \int_0^W C(x)\, \mathrm{d}x$. The average Rayleigh wave speed and the average longitudinal wave speed were found to be 2285 and 1007 m/s, respectively, for the graded foam samples and were 2256 and 999 m/s, respectively, for the 0.25 volume fraction homogeneous sample.
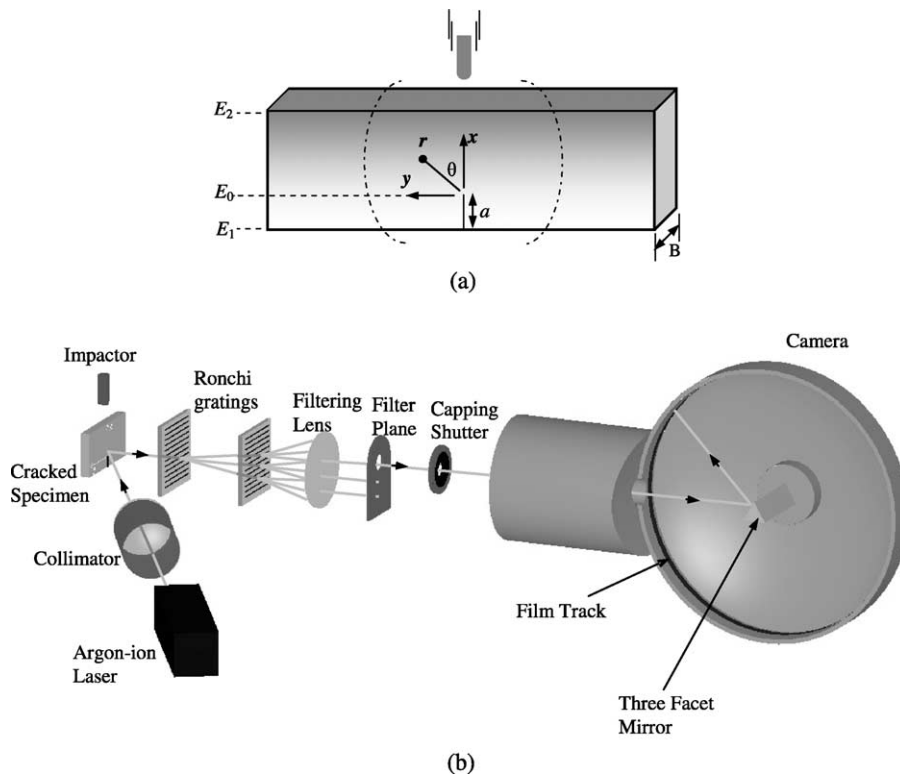
Fig. 2. Schematic of the (a) specimen and loading configuration, (b) experimental set-up for reflection CGS and high-speed photography.

The specimen surfaces were specially prepared to produce a specularly reflective region around the crack tip, on the 152 mm × 42 mm faces of the samples, for optical intereferometry. This was done by transferring a thin layer of aluminum in the region of interest. An optical flat was first coated with a few nanometers thick layer of aluminum film using vacuum deposition technique. This layer was then transferred to the specimen surface using a few drops of epoxy (same as the matrix material of the syntactic foam). Once the epoxy was cured, the glass disc was pried-off, leaving the specimen surface coated with a specularly reflective layer. The thickness of the epoxy-aluminum layer was about 8 μm, very small compared to the sample thickness.

2.2. Experimental set-up

The optical method of coherent gradient sensing (CGS) (Tippur et al., 1991) was used in this study to perform real-time measurement of instantaneous surface deformations around the crack tip during the dynamic event. A schematic of the optical set-up is shown in Fig. 2(b). The measurement system consisted of an impactor, pulse-laser, CGS interferometer and a continuous access high-speed camera. During the experiment, a pneumatically operated hammer with a steel cylindrical head having a hemi-spherical tip (radius 12.7 mm) was launched towards the specimen (speed ∼5.8 m/s). During its descent, the hammer first triggered a photodetector to open a capping shutter located in front of the high-speed camera, allowing light to reach its internal cavity. Subsequently, the tup impacted the specimen. An adhesive-backed copper

tape placed on the top edge of the specimen closed an electric circuit when contacted by the hammer. This initiated a series of laser pulses for a duration corresponding to a single sweep of the laser beam on the film track. The light entering the camera was then reflected-off of a spinning three-facet mirror mounted on a turbine shaft. The reflected light beam was swept on the film held stationary in a film track as discrete images. At the end of that period, the capping shutter was closed to prevent over-writing on the film. In the current experiments, the laser pulse was repeated every 5 μs with a pulse width of 50 ns and a total re-cording duration of ≈320 μs. For the settings used, ≈70 images were written over a 270° angle at a rate of 200,000 frames per second. The Argon-ion laser beam ($\lambda = 514$ nm) was expanded and collimated to il-luminate a circular spot of ∼50 mm diameter on the specimen. The reflected light beam, containing in-formation about the local out-of-plane deformations of the surface from its original state of flatness, was then transmitted through a pair of Ronchi gratings to shear the object wave front laterally perpendicular to the grating lines. All the diffracted wave fronts were then collected by a positive lens and displayed as a linear array of spots on the focal plane, where either the +1 or −1 diffraction orders were filtered and imaged. The 'camera', comprising of the positive lens and the image plane, was kept focused on the object surface at all times. The resulting fringes represent surface slopes in the x-direction (along the crack line and perpendicular to the grating lines), and are described by the governing equation of reflection CGS,

$$\frac{\partial w}{\partial x} \approx \frac{\delta w}{\delta x} = \frac{Np}{2\Delta}, \quad N = 0, \pm 1, \pm 2, \ldots, \tag{1}$$

where N denotes fringe orders, p is the pitch of the gratings (25 μm), Δ is the grating separation distance (49 mm) and $\delta(\cdot)$ is the difference operator. If plane stress conditions are assumed, the out-of-plane dis-placement w can be related to the in-plane normal stresses and elastic constants as,

$$\varepsilon_z \approx \frac{2w}{B} = -\frac{v}{E}(\sigma_x + \sigma_y) \tag{2}$$

where B is the thickness of the specimen. It should be noted that CGS being a measure of spatial derivative of stresses and deformations, uniform deformations and stresses, such as the T-stress term in the crack tip field description, are eliminated by the technique. This is beneficial in fracture mechanics since it allows an accurate determination of crack tip fracture parameters using K-dominant terms alone.

2.3. Optical results

2.3.1. Homogeneous foam sheets

The fringe patterns representing contours of constant surface slopes around the crack tip of the homo-geneous volume fraction ($= 0.25$) sample were captured every 5 μs for a total duration of over 300 μs. A few select fringe patterns representing contours of $\delta w/\delta x$ from one of the experiments is shown in Fig. 3. The fringes have a resolution of ≈0.015 deg/fringe and a line drawn parallel to the crack is located at a distance of 10 mm from the crack line. In these images, the impact point is located at the top of each frame where the hammer impacted the specimen on the 152 mm × 8.8 mm face symmetrically at a point opposite to the crack tip location. Highly discernable fringes on the specimen surface near the impact edge are clearly evident while the crack tip region is nearly free from significant deformations (fringes) at early times. With the passage of time, as the stress waves reach the crack tip, deformations increase until crack initiation and growth occurs. The shape of the crack tip interference pattern is the standard tri-lobed pattern of an elastic mode-I crack, with symmetric fringe orientation relative to the crack plane and three equally dominant lobes ≈120° apart. Among the selected fringe patterns shown in Fig. 3 is the one at 135 μs that corresponds to post-initiation event. In this image, the unloading surface wave emanating from the crack tip is clearly seen as a circular discontinuity, centered at the initial crack tip, in otherwise continuous fringe pattern. By measuring the location of the surface wave boundary in the neighboring frames, it was concluded that this
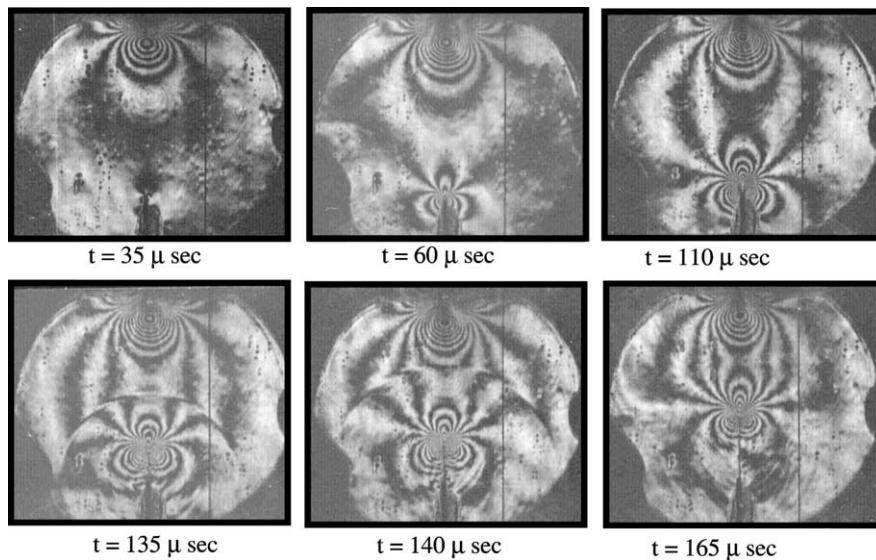
Fig. 3. Selected CGS interferograms representing contours of $\delta w/\delta x$ in a syntactic epoxy foam (volume fraction $= 0.25$) sheet impact loaded on the edge opposing the crack tip. Fringe sensitivity $\sim$0.015 deg/fringe, the vertical line parallel to the crack in each case is at a distance of 10 mm.

is the unloading Rayleigh wave originated from the initial crack tip at crack initiation. The fringe patterns at later times correspond to a dynamically growing mode-I crack in the specimen.

2.3.2. Functionally graded foam sheets

The optical results for the two different cases of functionally graded foams namely, one with a crack on the compliant side and the other with a crack on the stiffer side, are shown in Fig. 4(a) and (b), respectively. These two sequences of fringe patterns correspond to situations when the sample was impacted on the edge opposing the cracked side as in the homogeneous case. That is, the sample with a crack on the compliant side was impacted on the stiffer side and vice-versa. Similar to the homogeneous sample, here again the fringe patterns corresponding to the early times following impact indicate surface deformations in the central region near the impact point. At subsequent times, crack initiation and growth can be seen in both examples along with evidence of emanating surface waves after crack initiation. Following crack initiation and during dynamic growth, although the fringe patterns are generally symmetric about the crack plane, qualitative differences in the shape and size of the crack tip fringe lobes relative to each other can be clearly observed. For example, the fringe lobes ahead of the dynamically growing crack tip in case of the graded sample with $E_2/E_1 > 1$ is noticeably smaller compared to the ones for the case of $E_2/E_1 < 1$. These differences would affect the values of the crack tip fracture parameters to be quantified in the next sections.

2.4. Crack initiation and growth histories

Using these fringe patterns, instantaneous crack tip location in all the three cases were determined, and are shown in Fig. 5(a). The crack initiated at 95, 120, and 135 µs, respectively, in the graded foam with crack on the compliant side, homogeneous foam, and graded foam with crack on the stiff side. It should be noted that the crack initiation time was recorded from the interferograms to an accuracy of 5 µs, corresponding to the framing rate of the high-speed camera. Within the accuracy of measurements, it should be
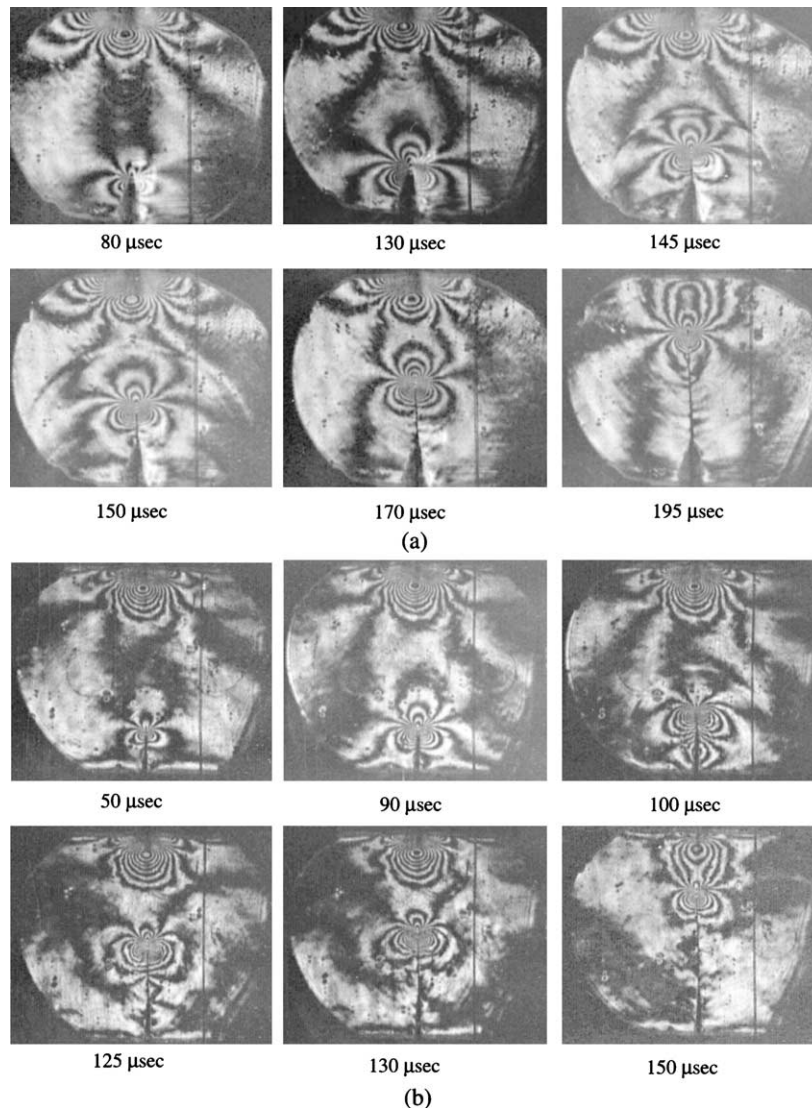
Fig. 4. Selected CGS interferograms representing contours of $\delta w/\delta x$ in functionally graded epoxy syntactic foam sheet impact loaded on the edge opposing the crack tip. Fringe sensitivity $\sim$0.015 deg/fringe, the vertical line parallel to the crack in each case is at a distance of 10 mm. (a) Crack on the stiffer $E_2/E_1 < 1$, crack initiation time, $t_i \sim 135$ μs, (b) crack on the compliant side $E_2/E_1 > 1$, crack initiation time, $t_i \sim 95$ μs.

noted that the crack initiation occurs earlier in the graded foam with crack on the compliant side when compared to the one on the stiffer side. This is due to the coupled effects of the local crack initiation toughness of the material and the gradations in the elastic and physical properties, which affect wave propagation patterns. This observation is consistent with those of Rousseau and Tippur (2001) who have recently studied solid glass-filled epoxy functionally graded materials (FGMs). The crack initiation time for the homogeneous sample is in between the ones for the two graded foams. The differences are particularly significant given the average wave speeds over the width of the samples are nearly same as described below.
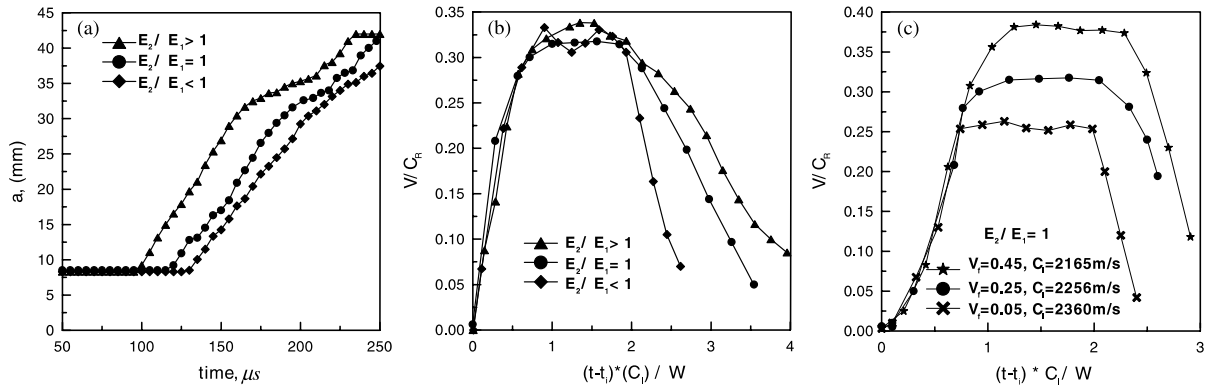
Fig. 5. Crack growth behavior in graded foam specimens under impact loading. (a) Crack growth history, (b) normalized crack speed (V) histories (t = time from impact, t_i = time at crack initiation, and $C(x)$ is local wave speed, subscripts l, R = longitudinal and Rayleigh wave speeds, respectively, W = sample width), (c) normalized crack speed in homogeneous foam sheets.

From the crack tip location histories, crack speeds were determined using forward difference calculations. These are shown in Fig. 5(b). The crack speeds are normalized using the *local* values of the Rayleigh wave speeds. As can be seen from the figure, crack growth pattern in each case is one of sudden acceleration ($\sim 13 \times 10^6$ m/s^2) after crack initiation to $\approx 32\%$ of the *local* Rayleigh wave speeds ($C_R(x)$). This is followed by a nearly constant crack speed for the duration of ≈ 40 μs (nondimensional time duration of 0.5–2). Crack deceleration in each case is seen following this period of steady state crack growth. Interestingly, decelerations are noticeably different in these cases within the window of observation. The deceleration for the graded foam sample with the crack initially located on the stiffer side is higher than the one with the crack on the compliant side. The homogeneous sample has a response bounded by those for the graded foams. Potential influence of in-plane crack tip constraint is used to explain this observation in the subsequent sections.

For comparison purposes, the crack speed histories from a complementary investigation (El-Hadek and Tippur, 2001) on the influence of pore volume fraction on dynamic crack growth behavior in *homogeneous* epoxy syntactic foams is shown in Fig. 5(c). Results for three cases with pore volume fraction of 0.05, 0.25, and 0.45, are included. Evidently, crack initiates earlier in the foam with the highest volume fraction of microballoons, $V_f = 0.45$, followed by the ones with 0.25 and 0.05, respectively. This is consistent with the monotonically decreasing crack initiation toughness values for this material shown in Fig. 12(c). Further, in each case, there is a rapid acceleration of the crack to $\approx 13 \times 10^6$ m/s^2, following initiation with a nearly constant crack speed attained for a short duration of 30–40 μs (nondimensional time duration of 0.5–2) before rapid deceleration as the crack encounters reflected stress waves from the specimen boundaries. These behaviors are same as the ones seen for the graded foams. From these results it is also evident that the samples with higher volume fraction of microballoons attain higher crack speeds between $0.25C_R$ to nearly $0.4C_R$. This is unlike the response of the graded foams wherein maximum attained crack speed was $\approx 0.32C_R$ in both cases. Another interesting difference is, unlike in the graded foams, the crack deceleration in the window of observation appears to be nearly same in all the three homogeneous cases.

2.5. Measurement of dynamic stress intensity factors

The crack tip stress intensity factors were extracted from the interference patterns using over-deterministic least-squares analysis of optically measured surface slope data in conjunction with crack tip field descriptions available at the moment for graded materials. The pre-crack initiation interferograms were

analyzed using asymptotic crack tip expressions for stresses and displacements in planar nonhomogeneous elastic body. Using asymptotic analysis, the first two terms of such a description for the sum of the in-plane normal stresses near a quasi-statically loaded mode-I stationary crack in a nonhomogeneous sheet have been shown to be of the form (Eischen, 1987),

$$(\sigma_x + \sigma_y) = (C_0 r^{-1/2} f_0^{I}(\theta) + C_1 r^0 f_1^{I}(\theta)) + \mathrm{O}(r^{1/2}), \tag{3}$$

where (r, θ) denote crack tip polar coordinates, f_0^{I}, f_1^{I} are angular functions, and C_0 and C_1, are the coefficients of the expansion with $C_0 = K_I/\sqrt{2\pi}$, K_I being the mode-I stress intensity factor, and C_1 represents the so-called T-stress since f_1^{I} is unity for mode-I. It should be noted that the angular functions for the first two terms in Eq. (3) are identical to the ones for a homogeneous counterpart. Using plane stress assumptions, out-of-plane displacement w can be related to the in-plane stresses using, $\varepsilon_z \approx 2w/B = -(v_0(\sigma_x + \sigma_y)/E_0)$ where B is the initial thickness of the sheet and E_0, v_0 denote crack tip Young's modulus and Poisson's ratio, respectively. Eq. (3) was used for determining stress intensity factors from the interferograms with an implicit assumption that all inertial effects enter the analysis through coefficients of the asymptotic field. That is, instantaneous $K_I \equiv K_I^{d}(t)$ where the superscript d represents pre-crack initiation stress intensity factor.

The options available for analyzing post-crack initiation interferograms are discussed next. Asymptotic expression for a steadily growing mode-I crack in a nonhomogeneous material with a unidirectional (x- in this case) variation of material properties is given to be of the form (Parameswaran and Shukla, 1999),

$$w(r, \theta; t) = \frac{-vB}{2(1 + v)(1 - 2v)} \left[A_0(t) r_1^{-1/2} \cos \frac{\theta_1}{2} + A_1(t) + A_2(t) r_1^{1/2} \cos \frac{\theta_1}{2} - \frac{\alpha}{4\alpha_1^2} A_0(t) r_1^{1/2} \cos \frac{3\theta_1}{2} \right.$$
$$\left. + \frac{2\alpha\alpha_s}{(k + 2)(\alpha_1^2 - \alpha_s^2)} B_0(t) r_s^{1/2} \cos \frac{\theta_s}{2} \right], \tag{4}$$

where,

$$k = \frac{\lambda_0}{\mu_0}, \quad \alpha_1 = \sqrt{1 - \frac{\rho_0 c^2}{\mu_0(k + 2)}}, \quad \alpha_s = \sqrt{1 - \frac{\rho_0 c^2}{\mu_0}}, \quad r_{1;s} = \sqrt{x^2 + \alpha_{1;s}^2 y^2}, \quad \theta_{1;s} = \tan^{-1} \frac{\alpha_{1;s} y}{x},$$

$$A_0 = \frac{(1 + \alpha_s^2)(1 - \alpha_1^2)}{4\alpha_s\alpha_1 - (1 + \alpha_s^2)^2} \frac{K_I^{D}}{\mu_c \sqrt{2\pi}}, \quad B_0 = \frac{2\alpha_1}{1 + \alpha_s^2} \frac{1 - \alpha_s^2}{1 - \alpha_1^2} A_0.$$

In the above equation, coefficients A_0, A_1 and A_2 are the unknown coefficients of the asymptotic expansion with A_0 proportional to the stress intensity factor K_I^{D} with superscript 'D' representing a dynamically growing crack, A_1 and A_2 are higher order coefficients with A_1 being the dynamic counterpart of the so-called T-stress defined under quasi-static conditions. Also, λ is the first Lamé's constant, $\mu_c = \mu_0 \exp(\alpha c t)$ is the shear modulus with the subscript '0' representing the value at the crack tip, c is the crack speed and α is the nonhomogeneity parameter (having units of 1/length) based on an *exponential description* of the spatial variation of shear modulus along the direction of crack growth, α is a positive or a negative constant representing material nonhomogeneity for increasing and decreasing modulus ahead of the crack tip, respectively. Evidently, as the material gradient parameter α becomes zero, the equations reduce to that of its homogeneous counterpart (Freund and Clifton, 1974). It should be emphasized here that the assumed spatial variation of density in the derivation of Eq. (4) is of the form $\rho_c = \rho_0 \exp(\alpha c t)$ and has identical nonhomogeneity parameter as that of the shear modulus variation. In view of this, two observations were made prior to using asymptotic expressions in Eq. (4) before analyzing the interferograms: (i) The requirement that nonhomogeneity parameter that describes both shear modulus and mass density be the same is quite restrictive for particulate compositions and foams. In the present case, the graded foams have a spatial variation of Young's modulus (Poisson's ratio is approximately constant, between 0.35 ± 0.01) and

density as shown in Fig. 1(b). The best exponential curve fits (not shown) of these variations yielded significantly different nonhomogeneity parameters $\alpha \approx -0.023$ mm^{-1} and -0.012 mm^{-1} for Young's modulus and density, respectively. (ii) In an earlier dynamic crack growth study involving solid-glass spheres suspended in a polymeric matrix (Rousseau and Tippur, 2001), Eq. (2) was used with and without ($\alpha = 0$) the nonhomogeneity parameter and the differences were found to be relatively small (<5%), for nonhomogeneity parameters of the same order. In view of these, it was deemed reasonable to evaluate dynamic stress intensity factors in the close vicinity of the crack using the first two terms of Eq. (4) with an implicit understandingthat a locally homogeneous material behavior is acceptable. Further, by doing so one can circumvent the difficulty posed by the last term in Eq. (4), which becomes unbounded as $c \rightarrow 0$, as explained in Rousseau and Tippur (2001).

For the optical analysis, fringes around the crack tip in graded sheets were digitized in a region $0.35 < r/B < 0.5$, and $90° < |\theta| < 135°$ to get fringe order N, and fringe location (r, θ) data. The region of choice for analyzing the $\delta w / \delta x$ optical data is known to be least influenced by triaxial effects for a mode-I crack tip (Tippur et al., 1991). The analysis of the optical data consisted of minimizing the least-squares error between the optical measurements (Eq. (1)) and the field description (Eqs. (3) or (4)). The details of such a procedure can be found in Tippur et al. (1991) and Tippur and Xu (1995).

2.6. Stress intensity factor histories

The stress intensity factor histories for the two graded and one homogeneous foam configurations are shown in Fig. 6(a)–(c). The symbols represent experimental measurements and the solid lines are from numerical simulations to be discussed in the subsequent sections. The stress intensity factors increase monotonically in each case until crack initiation. The crack initiation in the graded foam with a crack on the compliant side occurred at 95 μs, earlier than its counterpart with the crack on the stiffer side at 135 μs. The crack initiation time for the homogeneous counterpart with 25% volume fraction of microballoons is in between the two graded foam cases. The rates of increase of stress intensity factors up to crack initiation, K_I^d, in these three cases are also somewhat different. Evidently, the estimated time rate of increase of K_I^d for the case with the crack on the stiffer side ($\approx 33 \pm 2$ MPa $\sqrt{m}$/ms) is lower than that for the one with a crack on the compliant side ($\approx 42 \pm 2$ MPa $\sqrt{m}$/ms). These differences are attributed to the differences in the stress wave propagation patterns due to compositional grading in the samples. The lower crack tip loading rate could also explain crack deceleration in case of the FGM with the crack on the stiffer side since one can idealize crack growth as a series of stationary but dynamically loaded cracks of different lengths.

The post-crack initiation stress intensity factors K_I^D for the two graded sheets also show substantial differences. The instantaneous values of K_I^D are oscillatory due to the discrete wave reflections driving the crack forward. The measured values of K_I^D show an increasing trend following crack initiation when the crack is located on the compliant side. As the crack propagates in this case, it grows into the material having its local value of crack initiation toughness higher than its previous location and the measurements reflect this. On the contrary, the K_I^D values for the case of the graded foam with crack on the stiffer side shows a decreasing trend after crack initiation for the duration of the study. Interestingly, within the accuracy of measurements, the K_I^D values for both cases at $a/W = 0.5$ (where the volume fractions are identical at 25% in both cases) are nearly same (1.32 ± 0.05 MPa $\sqrt{m}$) suggesting that the dominant influence of local fracture toughness during crack growth in graded samples. In each case, K_I^D values could not be analyzed when the crack got close the impact location (edge) due to the severe interactions between the impact point and the crack tip. In comparison to the two graded foams, the post-crack initiation data of K_I^D for the homogeneous foam, however, shows an oscillatory but nearly constant value during the event. The dynamic fracture toughness K_I^D is plotted against instantaneous crack speed in Fig. 7 for the two graded foams. It should be noted here that both the axes of these plots are determined experimentally and hence susceptible to measurement errors. Hence, they show a greater degree of scatter. Within this scatter,
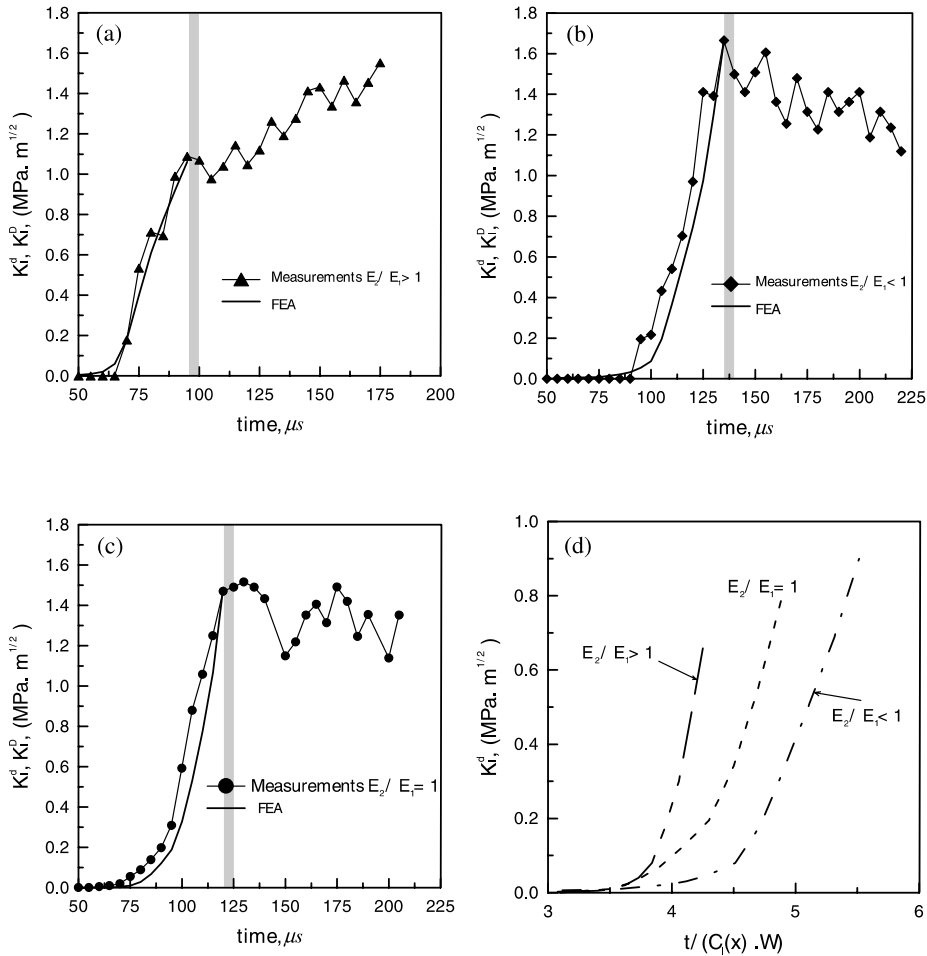
Fig. 6. Measured and computed (FEA) mode-I dynamic stress intensity factor histories for (a) graded foam with crack on the compliant side $E_2/E_1 > 1$, (b) graded foam with crack on the stiff side $E_2/E_1 < 1$, (c) homogeneous 0.25 V_f foam, and (d) an enlarged view of the computed K_I^d variations with normalized time for graded and homogeneous foams. K_I^d, K_I^D are pre- and post-crack initiation stress intensity factors, respectively. The shaded band corresponds to crack initiation time.

the measured K_I^D data show the following trends. The post-crack initiation data points, sequentially numbered in Fig. 7(a) and (b), are plotted for the two compositionally graded foam cases. The numbering of the data is used to follow the sequence of events during crack growth. The instantaneous crack speeds have been normalized by the local values of the Rayleigh wave speed ($C_R(x)$) for comparative purposes. The K_I^D values show a small increase as the crack initiates on the compliant side and accelerates to the stiffer side (points 1–5). As the crack speed reaches the maximum value (points 6–12) of the event window, the K_I^D values continue to increase. The increasing trend for K_I^D continues even as the crack begins to decelerate (points 12–17). For the case of the graded foam with crack on the stiffer side, the sequence of events essentially shows an opposite trend. The K_I^D values show a decreasing trend after crack initiation as the crack accelerates (points 1–5) towards the compliant side. As the crack speed reaches maximum speed (points 6–11), a noticeable drop in the fracture toughness followed by a nearly constant value with a small decreasing bias (points 11–15). For comparison purposes, a plot of K_I^D as a function of crack speed in homogeneous
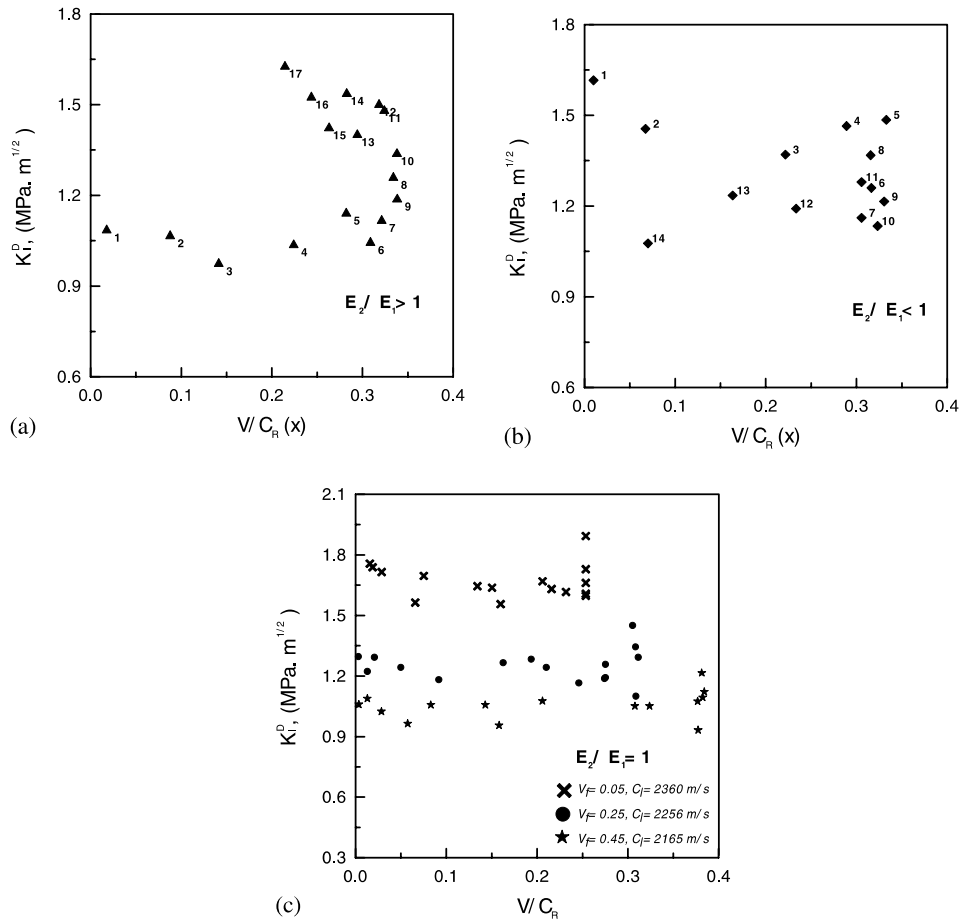
Fig. 7. Variation of dynamic SIF with crack velocity (a) crack on the compliant side, (b) crack on the stiffer side of the graded foam, and (c) homogeneous foam of three different volume fractions (V_f).

syntactic foams of three different volume fractions is shown in Fig. 7(c). Evidently, within the experimental scatter, K_I^D values are essentially constant over the entire range of crack velocities for three difference volume fractions of microballoons. This suggests that the local values of critical K_I^D control the crack growth behavior in the present case where the material does not show any significant velocity dependence during dynamic crack growth. The K_I^D–V variations shown in Fig. 7(a) and (b) can hence be attributed entirely to the influence of functional grading in the foam sheets.

3. Computations

Finite element simulations were carried out for supplementing optical measurements where needed. The simulations were used to (a) validate plane stress approximations employed while analyzing the optical data and, (b) gain additional insight into the differences in the crack tip loading rates observed in the two graded configurations using in-plane constraint differences due to compositional gradients. The former was accomplished by examining the crack tip triaxiality in the presence of compositional gradients while the latter

required evaluation of the so-called T-stress for the FGM configurations. It should be pointed out that being a surface slope measurement technique, CGS eliminates the T-stress term in the asymptotic expansion and had to be computed using finite element models.

3.1. Crack tip triaxiality (plane strain constraint)

First, 3-D elasto-static finite element simulations were performed to ensure the validity of plane stress assumptions used while analyzing the optical data in the finite thickness samples used in this study. Due to the symmetry of the problem about the crack plane and the mid-plane of the sample, one-quarter model was studied by imposing appropriate boundary conditions on the planes of symmetry. A schematic of the one-quarter model is shown in Fig. 8. The model consisted of eight-node brick elements, with $\approx 79{,}000$ elements and 84,000 nodes having three degrees-of-freedom per node. The crack tip region was highly refined in order to capture the details of the crack tip deformations accurately. The sample thickness was
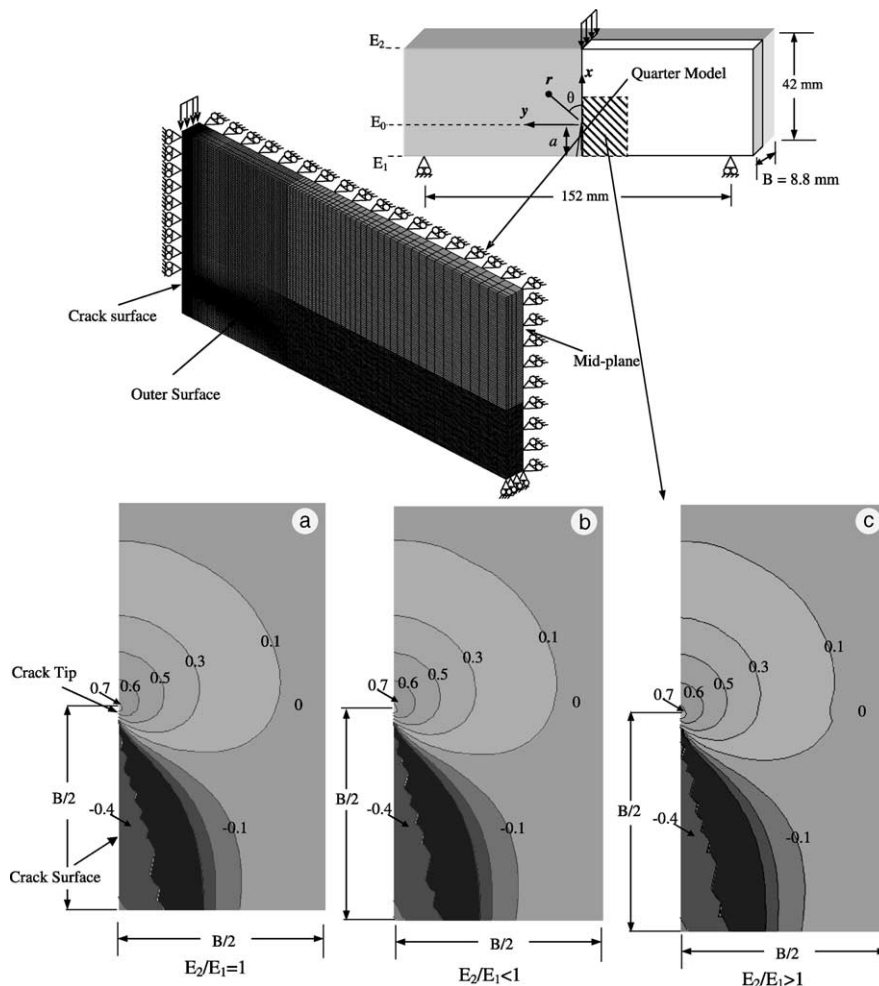

Fig. 8. Examination of crack tip triaxiality in static three-point bending using plane strain constraint parameter $\sigma_z / \nu(\sigma_x + \sigma_y)$ on the mid-plane of (a) homogeneous and (b, c) graded foam sheets with crack stiffer and compliant sides respectively.

discretized into eight layers with finer layers adjacent to the surface of the model and thicker layers located close to the mid-plane. No special singular elements were used near the crack tip region. The variation of Young's modulus in the x-direction, same as the one used in the experiments, was applied to the elements using the technique developed by Rousseau and Tippur (2001). The value of Poisson's ratio was kept constant at 0.35 over the entire model. The model was subjected to symmetric three-point bending and the nodal values of stresses were retrieved for further analysis. The plane strain constraint defined by the parameter $(\sigma_{33}/v(\sigma_{11} + \sigma_{22}))$ is an indicator of the degree of triaxiality near a crack tip. The magnitude of the parameter is unity in regions where deformations can be approximated by plane-strain conditions and approach zero where plane-stress conditions prevail. Many investigators have previously used this parameter to investigate crack tip triaxiality in homogeneous materials (Rosakis and Ravi-Chandar, 1986) as well as in bimaterials (Sinha et al., 1997). In the present study, crack tip triaxiality effects due to compositional gradients were examined using this parameter. In Fig. 8(a)–(c), contours of plane strain constraint near the crack tip vicinity are shown for the two graded and a homogeneous foam cases. These correspond to compositionally graded foam cases with crack on the stiffer and compliant sides of the three-point bend beam and for the homogeneous beam. In both the functionally graded foam cases, the crack tip triaxiality contours are essentially identical to the one for the homogeneous foam. That is, the compositional grading has not evidently altered the nature of crack tip triaxiality. Therefore, adopting the existing knowledge about the regions of dominant 3-D deformations in homogeneous solids should suffice in the graded material optical data analysis as well. Accordingly, plane stress approximation is generally reasonable in regions outside $r/B > 0.5$ ahead of the functionally graded crack tip where B is the thickness of the sheet. More importantly, plane stress conditions can be realized at much smaller distances behind the crack tip in the region $r/B > 0.30$ and $90° < \theta < 135°$. Thus, the optical data analyzed in this region using plane stress assumptions is deemed reasonable.

3.2. Stress intensity factor histories

Two-dimensional elasto-dynamic computations corresponding to the experimental situations were carried out for determining stress intensity factor histories in graded foams. The finite element simulations included 2-D plane-stress analysis of symmetrically loaded free–free edge cracked beams subjected to single point impact. The numerical model consisted of about 10,000 8-noded elements with $\approx$16,000 nodes and two degrees-of-freedom per node. Due to the symmetry, only one-half of the model was simulated with symmetry boundary conditions on the planes of symmetry. An 8 mm long crack ($a/W \sim 0.2$) was simulated by removing all the nodal constraints along the plane of symmetry over the crack length. The crack tip region was highly discretized with the elements surrounding the crack tip of size $\approx 10^{-4}a$. The sample loading was simulated by imposing displacement boundary conditions corresponding to a rigid projectile impact with a velocity of 5.8 m/s at the impact location. The explicit integration scheme used a time increment of 0.01 μs over a period of 150 μs to simulate pre-crack initiation response of the sample. [1] The compositional grading of the numerical model was implemented by varying the Young's modulus and density over the entire model in the x-direction. The variation of the properties in the model corresponds to the values shown in Fig. 1(a) and (b). The Poisson's ratio in both the models were kept constant at 0.35. A homogeneous sample with material properties corresponding to that of a 25% volume fraction of microballoons was also simulated for comparative purposes. All other simulation parameters were identical to those used for functionally graded samples.

---

[1] Benchmark simulations were carried out to ensure the fidelity of the computations using the example problem reported in Rousseau and Tippur (2001). The details of the benchmark analysis are avoided here for brevity.

Crack opening displacements along the crack flanks were used for extracting instantaneous $K_{\mathrm{I}}^{\mathrm{d}}$ values based on locally homogeneous material behavior. Using the first three terms of the Williams' asymptotic expansion for the crack opening displacements, apparent stress intensity factors can be expressed as,

$$\widehat{K}_{\mathrm{I}}^{\mathrm{d}}(t) = K_{\mathrm{I}}^{\mathrm{d}}(t) - Dr, \tag{5}$$

where

$$\widehat{K}_{\mathrm{I}}^{\mathrm{d}}(t) = \sqrt{\frac{2\pi}{r}} \frac{E_0 \delta_y(t)|_{\theta=\pm\pi,}}{8}$$

is the *apparent* stress intensity factor, δ_y is the crack opening displacement, $K_{\mathrm{I}}^{\mathrm{d}}$ is the value of the crack tip stress intensity factor, E_0 is the dynamic Young's modulus at the crack tip and D is a higher order coefficient. For each time instant, values of $\widehat{K}_{\mathrm{I}}^{\mathrm{d}}$ were plotted against r and the extrapolated value $K_{\mathrm{I}}^{\mathrm{d}} = \lim_{r\to 0} \widehat{K}_{\mathrm{I}}^{\mathrm{d}}$ was evaluated as the instantaneous stress intensity factor. The values of $K_{\mathrm{I}}^{\mathrm{d}}$ were determined for time steps corresponding to the framing rates used in the experiments for comparison purposes. The computed mode-I dynamic stress intensity factor $K_{\mathrm{I}}^{\mathrm{d}}$ history, *up to crack initiation*, for the two graded foam cases are shown in Fig. 6(a) and (b). In both the cases the agreement between the experimental measurements and computations are very good.

The finite element computations were used to obtain details of the crack tip loading rates in each case. The rate of increase of dynamic stress intensity factors prior to crack initiation ($\mathrm{d}K_{\mathrm{I}}^{\mathrm{d}}/\mathrm{d}t$) calculated experimentally was observed to be different in the three cases, and hence details of the crack tip stress intensity factor history was evaluated in the nondimensional time range of 3–6 as shown in Fig. 6(d). From the finite element data, the $\mathrm{d}K_{\mathrm{I}}^{\mathrm{d}}/\mathrm{d}t$ variation in each case was quantified as 37 ± 3 MPa $\sqrt{\mathrm{m}}$/ms and 52 ± 3 MPa $\sqrt{\mathrm{m}}$/ms for the case with the crack on the stiffer side and compliant sides, respectively, while 44 ± 2 MPa $\sqrt{\mathrm{m}}$/ms in the homogeneous counterpart with 25% volume fraction of microballoons. These trends are similar to the experimental ones discussed earlier. A plausible explanation for this difference in the rate of increase of dynamic stress intensity factors prior to crack initiation is attempted next.

3.3. T-stress computations

In fracture mechanics, primary focus is often on the stress intensity factor as an engineering parameter that describes the amplification of the singular stress field ahead of the crack tip governing the fracture response. However, recent investigations (Fett, 1998) point to the significance of the nonsingular constant stress term (second term in Eq. (3) or (4)) or the so-called T-stress playing an important role in the fracture process. Similar realization about the inadequacy of J-integral alone as the elasto-plastic fracture parameter predates (Cotterell et al., 1985) its elastic counterparts where the effect of the second or the so-called Q-stress term has been recognized. Under small scale yielding conditions one can use T-stress in place of Q-stress as suggested by O'Dowd and Shih (1992). Until recently, this discussion was limited to quasi-static loading conditions and in the past few years the role of nonsingular stresses on fracture behavior under dynamic loading conditions has come under scrutiny as well. Koppenhoefer and Dodds (1996) studied Q-stress histories in cracked Charpy specimens and have observed relatively large negative Q-stresses over the entire loading history. Jayadevan et al. (2001) have put forward an interesting hypothesis that large negative T-stresses might be responsible for the increasing dynamic crack initiation toughness with loading rates commonly observed. All these investigations have focused on the nonsingular stress term effects in homogeneous cracked bodies. The role of T-stress on crack growth in functionally graded materials subjected to static loading has been addressed in a recent work by Becker et al. (2001). They have recognized the alterations elastic gradients could introduce on the T-stress and the resulting effect on crack kinking. To date, however, there has been no attempt to examine evolution of T-stress histories in dynamically loaded

functionally graded materials and its potential role in crack initiation and growth behavior. Accordingly, in this work T-stress histories for the two compositionally graded foam cases as well their homogeneous counterpart were computed and the results were correlated with the stress intensity factor histories and crack growth behaviors.

The T-stress computations were based on the existing crack tip field descriptions for the singular and first nonsingular terms in Eqs. (3) and (4). Two computational strategies, (a) stress difference method (Yang and Ravi-Chandar, 1999) and (b) interaction integral method (Kfouri, 1986) are available to compute instantaneous values of T-stress near the crack tip in graded and homogeneous samples. Due to the simplicity of implementation, the former method is used in this study after performing the necessary benchmark computations. The first two terms of the mode-I asymptotic stress fields for the functionally graded and homogeneous samples can be written as,

$$
\begin{Bmatrix} \sigma_x \\ \sigma_y \end{Bmatrix} \approx \frac{K_\mathrm{I}}{\sqrt{2\pi}} \cos\frac{\theta}{2} \begin{bmatrix} 1 - \sin\frac{\theta}{2}\sin\frac{3\theta}{2} \\ 1 + \sin\frac{\theta}{2}\sin\frac{3\theta}{2} \end{bmatrix} (r^{-1/2}) + \begin{bmatrix} T \\ 0 \end{bmatrix} (r^0)
\tag{6}
$$

The instantaneous T-stress values can then be computed as, $T = \lim_{r\to 0}(\sigma_x - \sigma_y)$.

The T-stress values were evaluated numerically using elasto-static plane stress finite element models of compositionally graded and homogeneous foam samples in three-point bending configuration (beam span = 154 mm). These simulations were used for benchmarking the T-stress evaluation procedure against existing data in the literature. The computed stress differences ahead the crack tip ($r, \theta = 0°$) were plotted close to crack tip. The data were normalized using stress intensity factor and crack length to get the so-called biaxiality parameter $\beta = T\sqrt{\pi a}/K_\mathrm{I}$. Fig. 9(a) shows the plot of β ahead of the crack tip for the homogeneous beam ($a/W = 0.2$). Evidently, in the region $0.2 < r/B < 0.75$ the biaxiality parameter is essentially constant and the extrapolated value to the crack tip yields a value of -0.241. This value of β is in excellent agreement with that reported by Kfouri (1986). Next, in Fig. 9(b) and (c) the values of the biaxiality parameters ahead of the crack tip for the two graded foam cases with the crack on the compliant and stiff sides, respectively, and subjected to three-point static bending is shown. As in the homogeneous case, again values of β ahead of the crack tip are once again nearly constant over $0.25 < r/B < 0.7$ and the extrapolated values for each are -0.184 for the case with the crack on the stiff side of the beam while it is -0.389 for the case with a crack on the compliant side. Interestingly, although the graded samples have identical loading and geometrical configurations, the T-stresses and hence the β values are substantially different relative to each other and the homogeneous sample. A compilation of such results along with the corresponding stress intensity factor computations for various a/W ratios are shown in Fig. 10. Computed K_I values (normalized by the homogeneous counterpart) shown in Fig. 10(a), and T-stresses were used to obtain the biaxiality parameters for each a/W ratio. The variation of β as a function of crack length is shown in Fig. 10(b). Also shown are the results from Kfouri (1986) for homogeneous samples as the broken line. This plot clearly shows the differences in the in-plane constraint the quasi-statically loaded crack tip experiences as a result of the compositional gradients in the two foam samples. Evidently, from Fig. 10(b) one can see that a crack tip located on the compliant side of the FGM loses its negative constraint at much shorter crack lengths than the one with the crack on the stiffer side. Except that these results do not include inertial loading effects, one could surmise that this difference is responsible for the differences in the crack growth characteristics in the two FGMs.

Having demonstrated the feasibility of evaluating the crack tip T-stresses in functionally graded foams under static loading, computations were undertaken for dynamic conditions as well. Following the procedure described above, the evolution of biaxiality parameter $\beta(t)$ was computed by post-processing stress data obtained from the elasto-dynamic simulations. For computing instantaneous values of $\beta(t)$, previously determined dynamic stress intensity factor histories in each case along with the instantaneous values of T-stress were used. Plots of $\beta(t)$ for the two graded foams and the homogeneous counterpart are shown in
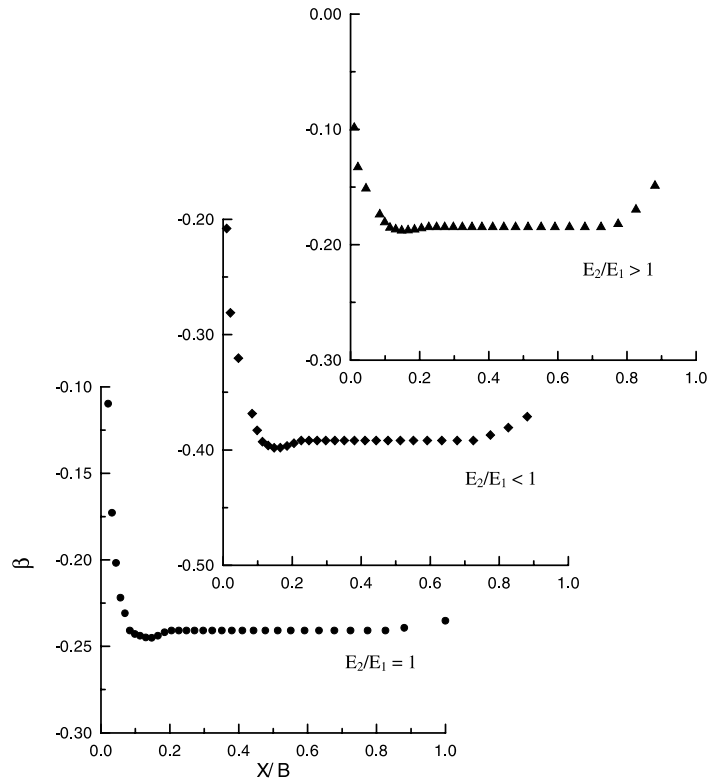
Fig. 9. Evaluation of the biaxiality parameter ($\beta = T\sqrt{\pi a}/K_1$) in homogenous, and graded foam sheets, using stress difference method for static three-point bending configuration ($a/w = 0.2$).
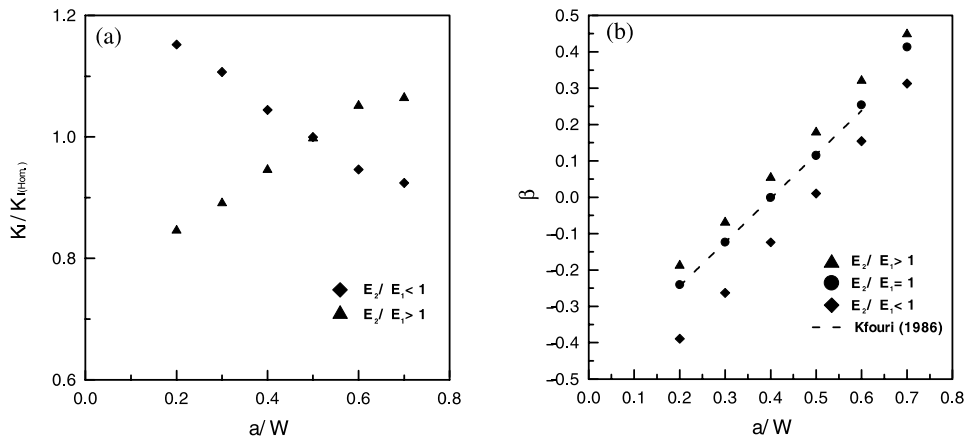

Fig. 10. (a) Computed static SIFs for various a/W ratios, (b) influence of compositional grading on the crack tip biaxiality parameter ($\beta = T\sqrt{\pi a}/K_1$) in three-point bending specimens.

Fig. 11. The plots are shown in the time window after a few wave reflections between the top and bottom edges of the samples and up to well after the experimentally observed crack initiation times. Evidently, the
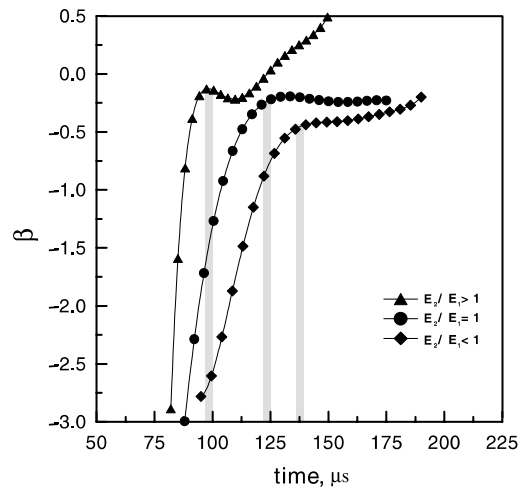
Fig. 11. Crack tip biaxiality ($\beta = T\sqrt{\pi a}/K_I$) histories in graded and homogeneous sheets subjected to one-point symmetric impact loading. The shaded band corresponds to crack initiation time.

biaxiality parameter becomes oscillatory at later times. Also, plotted is the experimentally determined values crack initiation time in each sample during the tests.

The values of $\beta(t)$ are strongly negative immediately after impact in each case compared to those close to crack initiation. As noted earlier in the quasi-static case, the $\beta(t)$ values for the case with crack on the stiffer side are strongly negative relative to its counterpart with the crack on the compliant side at all times. Also, significant are the rate of change of the biaxiality parameter $d\beta/dt$ for each case. Evidently, there is a direct correlation between the rate of crack tip loading (dK_I^d/dt) in Fig. 6(d) and $d\beta/dt$ in Fig. 11. Hence one could argue that the loss of in-plane crack tip constraint occurring earlier in the graded foam sample with the crack on the compliant side relative to the one with the crack on the stiffer side contributes to the higher crack tip loading rate and earlier crack initiation in the former. A second observation is about the rate of change of crack tip constraint $d\beta/dt$ in the two graded foams and the homogeneous counterpart. It should be emphasized that the values of $\beta(t)$ after the crack initiation time are not meaningful in Fig. 11 but are plotted only to suggest this second correlation between crack initiation and crack tip biaxiality. In each case, for both the graded foams as well as the homogeneous counterpart, crack initiation seems to have occurred when $d\beta/dt$ has approximately become zero. The significance of this observation may need further investigation to establish its generality and usefulness. Nevertheless, one could speculate that crack initiation might potentially be linked to crack tip biaxiality reaching a critical value for a given crack geometry.

4. Conclusions

Functionally graded epoxy foam sheets have been developed by spatially varying microballoons volume fraction in the mixture. The resulting graded foam sheets have a linear monotonic variation in volume fraction of the microballoons in the range of 0–45% over a length of 42 mm. The resulting spatial variation of Young's modulus and density is approximately two fold. The investigation has focused on the dynamic fracture behavior of these syntactic foams when subjected to low velocity impact loading. The research has
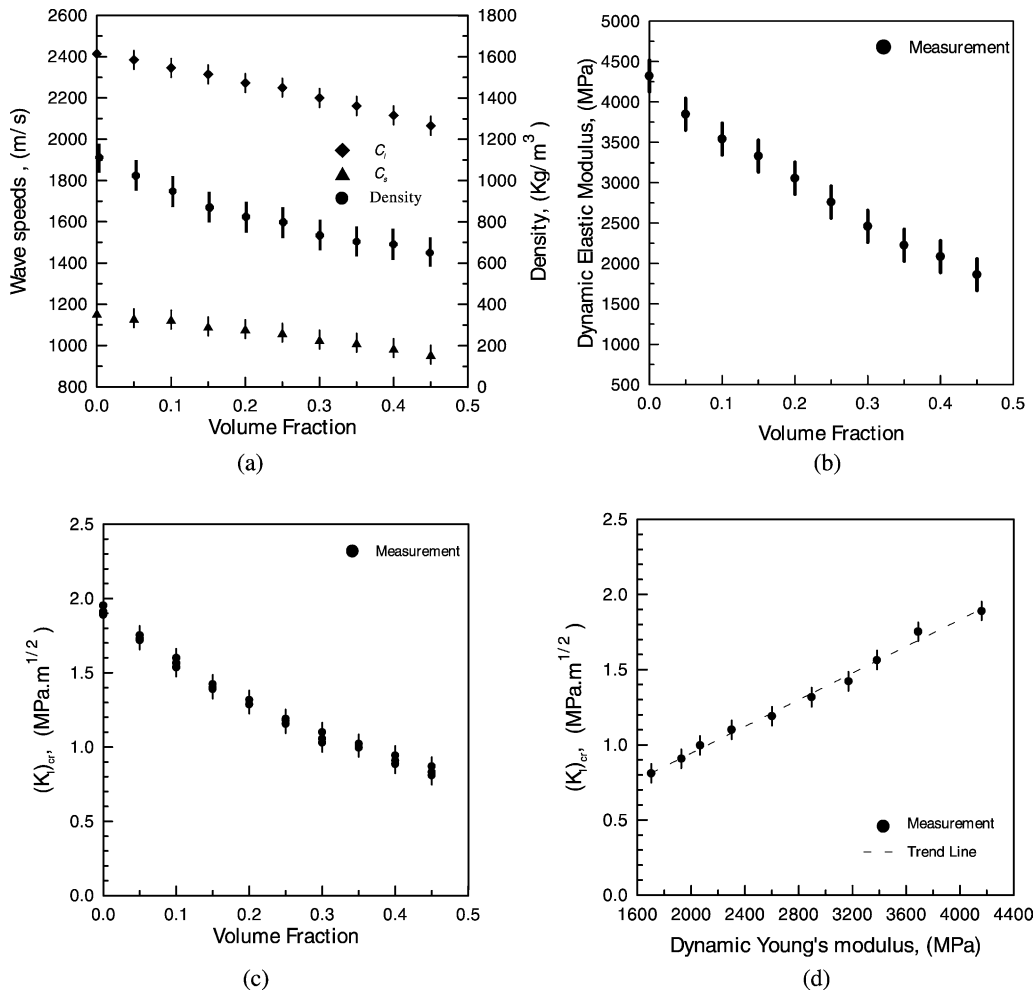
Fig. 12. Material properties of epoxy syntactic foams. Variation of (a) elastic wave speeds (C_l and C_s: longitudinal and shear wave speeds) and density, (b) dynamic Young's modulus, and (c) critical SIF, with microballoon volume fraction, (d) linear correlation between measured critical SIF and dynamic Young's modulus in syntactic epoxy foams.

also extended the optical method of reflection CGS and high-speed photography for mapping dynamic deformations near stationary and dynamically growing cracks in foams. The fracture behaviors observed during this investigation are summarized as follows:

- The crack growth pattern along the compositional gradient includes acceleration followed by nearly steady state growth and deceleration in the window of observation. The crack acceleration in three different cases (crack on the compliant side with impact on the stiffer side ($E_2/E_1 > 1$), homogeneous ($E_2/E_1 = 1$), and crack on the stiffer side with impact on the compliant side ($E_2/E_1 < 1$)) are similar with steady state crack growth occurring at a velocity of ~$0.32C_R$ The crack deceleration, however, shows differences with a higher deceleration in the graded foam with crack on the stiff side compared to the one with a crack on the compliant side. The response of the homogeneous sample is bounded by the two graded foam responses.

- The dynamic stress intensity factor histories prior to crack initiation in each case shows a rapid increase at different rates with the case with the crack on the compliant side experiencing higher rate of loading relative to the one with the crack on the stiffer side.
- Post-crack initiation stress intensity factor histories suggest increasing fracture toughness with crack growth in the sample having a crack on the compliant side while a decreasing trend is seen when the crack is located on the stiffer side. For the same loading configuration and specimen geometry, the homogeneous counterpart shows nearly constant fracture toughness during crack growth.
- Dynamic stress intensity factor variation as a function of crack velocity (V) shows increasing and decreasing trends in the graded foams with crack on the compliant and stiffer sides, respectively, although fracture toughness of the homogeneous foams have no significant crack velocity dependence. Since the dynamic fracture toughness (K_I^D) for homogeneous foams do not show any significant velocity dependence, the K_I^D vs. V variations in graded cases are entirely attributed to the compositional gradients.

Finite element simulations supplement the experiments in validating the plane stress assumptions used in the optical data analysis and in offering explanations for different crack tip responses observed in the graded foams. Some of the conclusions drawn from the numerical results when examined in conjunction with the measurements are summarized as follows:

- Three-dimensional elasto-static finite element analyses of the functionally graded single edge notched three-point bend configurations show crack tip triaxiality in terms of plane strain constraints is essentially identical to that of a homogeneous counterpart.
- The computed pre-crack initiation dynamic stress intensity factor histories obtained from plane-stress elasto-dynamic analyses of the two graded foams correlate well with the experimental measurements based on locally homogeneous material behavior.
- The computed biaxiality parameters β and its history ($\beta(t)$) for the case with a crack on the stiffer side are strongly negative compared to its counterpart with a crack on the compliant side at all times. This earlier loss of crack tip constraint in the latter case correlates with higher crack tip loading rate, crack initiation, and growth suggesting a strong link between in-plane constraint and fracture in graded materials.
- The rate of change of crack tip biaxiality parameter becoming stationary close to experimentally observed crack initiation times is observed in both the graded foam cases as well as in the homogeneous counterpart.

Acknowledgement

Appendix A

The dependence of longitudinal and shear wave speeds and density of the particular syntactic epoxy foam with volume fraction of microballoons is shown in Fig. 12(a). The wave speeds were measured using ultrasonic pulse-echo transducers of ≈2 mm radius. The wave speed measurements along with material density were used to evaluate Young's modulus and Poisson's ratio. Also, included in Fig. 12 are the results for Young's modulus and crack initiation toughness as a function of microballoon volume fraction in Fig. 12(b)

and (c), respectively. The crack initiation toughness values shown in Fig. 12(c) were obtained from a series of three-point bending tests on three-point edge cracked homogeneous beams tested using a drop tower with an impact velocity of 1.5 m/s. The crack initiation toughness data was determined by measuring critical load corresponding to crack initiation. Additionally, a linear relationship between dynamic Young's modulus and dynamic fracture toughness was found for these syntactic epoxy compositions, as shown in Fig. 12(d).

References

Bardella, L., Genna, F., 2001. On the elastic behavior of syntactic foams. Int. J. Solids Struct. 38, 7235–7260.

Becker, T.J., Cannon, RM., Ritchie, R.O., 2001. Finite crack kinking and T-stress in functionally graded materials. Int. J. Solids Struct. 38, 5545–5563.

Burcher, R., 1994. Concepts in Submarine Design. Cambridge University Press, Cambridge, NY.

Cotterell, B., Li, Q., Zhang, D., Mai, Y.W., 1985. On the effect of plastic constraint on ductile tearing in a structural steel. J. Eng. Fract. Mech. 21, 239–244.

El-Hadek, M., Tippur, H.V., 2001. Dynamic fracture behavior of syntactic epoxy foams: optical measurements and analysis. In: Proceedings of ASME-IMECE, CD-ROM vol. 1, Paper # AMD-24511.

El-Hadek, M., Tippur, H.V., 2002. Simulation of porosity by microballoon dispersion in epoxy and urethane: mechanical measurement and models. J. Mater. Sci. 37 (8), 1649–1660.

Eischen, J., 1987. Fracture of nonhomogeneous materials. Int. J. Fract. 34, 3–22.

Fett, T., 1998. T-stresses in rectangular plates and circular disks. J. Eng. Fract. Mech. 60, 631–652.

Freund, L.B., Clifton, R.J., 1974. On the uniqueness of plane elastodynamic solution for running cracks. J. Elasticity 4 (4), 293–299.

Gupta, N., Kishore, Sankaran, S., 1999. On the characterisation of syntactic foam core sandwich composites for compressive properties. J. Reinforced Plastics Compos. 18 (14), 1347–1357.

Huang, J., Gibson, L., 1993. Elastic moduli of a composite of hollow spheres in a matrix. J. Mech. Phys. Solids 41 (1), 55–75.

Jayadevan, K., Narasimhan, R., Ramamurthy, T., Dattaguru, B., 2001. A numerical study in dynamically loaded fracture specimens. Int. J. Solids Struct. 38, 4987–5005.

Kfouri, A.P., 1986. Some evaluations of the elastic T-term using Eshelby's method. Int. J. Fract. 30, 301–315.

Kim, H., Oh, H., 2000. Manufacturing and impact behavior of syntactic foam. J. Appl. Polym. Sci. 76 (8), 1324–1328.

Koizumi, M., 1997. FGM activities in Japan. Composites B 28, 1–4.

Koppenhoefer, K.C., Dodds, R.H., 1996. Constraint effects on fracture toughness of impact-loaded, precracked Charpy specimens. J. Nucl. Eng. Des. 162 (2–3), 145–158.

O'Dowd, N.P., Shih, C.F., 1992. Two parameter fracture mechanics: theory and applications. ASTM-STP 1207, 21–47.

Parameswaran, V., Shukla, A., 1999. Crack-tip stress field for dynamic fracture in functionally gradient materials. Mech. Mater. 31, 579–596.

Rizzi, E., Papa, E., Corigliano, A., 2000. Mechanical behavior of a syntactic foam: experiments and modeling. Int. J. Solids Struct. 37, 5773–5794.

Rosakis, A.J., Ravi-Chandar, K., 1986. On crack-tip stress state: an experimental evaluation of three dimensional effects. Int. J. Solids Struct. 22, 121–134.

Rousseau, C.-E., Tippur, H.V., 2001. Dynamic fracture of compositionally graded materials with cracks along the elastic gradient experiments and analysis. Mech. Mater. 33, 403–421.

Rousseau, C.-E., Tippur, H.V., 2001. Influence of elastic gradient profiles on dynamically loaded functionally graded materials: cracks along the gradient. Int. J. Solids Struct. 38, 7839–7856.

Scarponi, C., Briotti, G., Barboni, R., Marcone, A., Iannone, M., 1996. Impact testing on composites laminates and sandwich panels. J. Compos. Mater. 30 (17), 1873–1911.

Shutov, F., 1986. Syntactic polymer foams. Adv. Polym. Sci. 73/74, 63–123.

Sinha, J.K., Tippur, H.V., Xu, L., 1997. Interferometric and finite element investigation of interfacial crack tip fields: role of mode-mixity on 3-D stress variations. Int. J. Solids Struct. 34, 741–754.

Tippur, H.V., Xu, L., 1995. Measurement of interfacial fracture parameters using coherent gradient sensing (CGS). Strain 31 (4), 143–149.

Tippur, H.V., Krishnaswamy, S., Rosakis, A.J., 1991. A coherent gradient sensor for crack tip measurements: analysis and experimental results. Int. J. Fract. 48, 193–204.

Yang, B., Ravi-Chandar, K., 1999. Evaluation of elastic T-stress by stress difference method. J. Eng. Fract. Mech. 64, 589–605.